Microstructure, Mechanical Properties and Oxidation Behavior of Refractory Multi-Principal

Element Alloys by Laser Remelting and Conventional Manufacturing

Visharad Jalan¹, Seth Crawford¹, Sung-Heng Wu², Frank Liou², Haiming Wen^{1,3,*}

¹ Department of Materials Science and Engineering, Missouri University of Science and Technology,

Rolla, MO 65409, USA

² Department of Mechanical Engineering, Missouri University of Science and Technology, Rolla, MO

65409. USA

³ Department of Nuclear Engineering and Radiation Science, Missouri University of Science and

Technology, Rolla, MO 65409, USA

*Corresponding author: wenha@mst.edu; Tel.: +1-573-341-6167

Abstract

Refractory multi-principal element alloys (RMPEAs), HfNbTaTiZr, (HfNbTaTiZr)₉Cr and (HfNbTaTiZr)₉Al,

were manufactured using vacuum arc melting followed by laser-remelting to mimic additive

manufacturing. The microhardness of as-cast HfNbTaTiZr, (HfNbTaTiZr)₉Cr and (HfNbTaTiZr)₉Al

samples after arc melting was measured as 6.20, 7.63 and 6.89 GPa, respectively. After laser-remelting

and re-solidification, the hardness increased by ~30% for each composition; the hardest was

(HfNbTaTiZr)₉Cr measured at 9.60 GPa, and the softest was HfNbTaTiZr with a hardness of 8.42 GPa,

which was still harder compared to all the as-cast samples. The addition of Al and Cr led to enhanced

oxidation resistance for the respective RMPEA systems. The Al-containing composition showed the

best oxidation resistance for the as-cast samples; however, after laser remelting, the Cr-containing

RMPEA had the best overall oxidation resistance, and the increase in weight after oxidation dropped

by 42% when compared to that for the as-cast alloy. Laser remelting the RMPEAs led to an

1

improvement in mechanical properties; it also resulted in enhanced oxidation resistance for (HfNbTaTiZr)₉Cr. However, laser remelting barely changed the oxidation resistance for (HfNbTaTiZr)₉Al, and it decreased the oxidation resistance for HfNbTaTiZr. These phenomena are related to microstructure changes induced by the laser remelting/additive manufacturing as compared to conventional casting-based manufacturing.

1. Introduction

Throughout human history, there have been demands for better properties in metals and alloys such as ductility, high strength, lightweight, corrosion resistance etc. Multi-principal element alloys (MPEAs) are a novel class of metallic alloys that have emerged over the past two decades and have garnered significant attention due to their unique properties and potential applications. This class of alloys, unlike traditional alloys, have more than one principal component, usually five or more, in equiatomic or near-equiatomic concentrations. Incorporation of five or more principal elements contributes to the alloy's high entropy and disorder, which lead to their exceptional properties. The use of high melting point metals, such as molybdenum, tantalum, hafnium, in the synthesis of these MPEAs gives rise to another sub-class, called refractory multi-principal element alloys (RMPEAs). RMPEAs are characterized by their high melting points, excellent mechanical properties, and resistance to extreme conditions, making them potential candidates for high-temperature applications, such as in aerospace and energy industries. Nevertheless, RMPEAs tend to have poor oxidation resistance; therefore, it is important to study their oxidation behavior and try to improve their oxidation resistance. Such studies are very limited in the literature.

HfNbTaTiZr and similar compositions of RMPEAs have been previously studied, but most of the studies revolve around understanding the phase composition of the alloy and exploring the ambient-and-high temperature mechanical properties which are manufactured using conventional methods like

vacuum arc melting [1–3], powder metallurgy [4–6] etc. Additive manufacturing is an emerging manufacturing technology. It has short lead time from design to manufacturing. In addition, in comparison with conventional manufacturing techniques, additive manufacturing can produce complex geometries at no extra cost and with considerably less post-processing. In the past few years, direct metal deposition (DMD) and selective laser melting (SLM) processes, both of which are additive manufacturing techniques, have been employed to manufacture near-net-shape structures from RMPEAs [7–11]. Selective electron beam melting has also been utilized to additively manufacture RMPEAs [12]. However, most of these studies focused on the synthesis and preliminary structure-property characterization, whereas the impact of additive manufacturing on oxidation behavior has not been studied. This present study focuses on the systematic comparisons between RMPEAs manufactured using vacuum arc melting and those fabricated by additional laser remelting (i.e., an analog of additive manufacturing) with regard to microstructure, hardness, and oxidation behavior.

2. Materials and methods

Three compositions of RMPEAs were synthesized, namely, HfNbTaTiZr (C1), (HfNbTaTiZr)₉Al (C_Al) & (HfNbTaTiZr)₉Cr (C_Cr). These RMPEAs were arc-melted and cast, followed by surface laser remelting and re-solidification. Characterization and testing were performed in terms of microstructural development, micro-hardness, and oxidation behavior.

2.1. Arc melting and casting

For the synthesis of each of these RMPEA compositions, high purity (> 99.5%) constituent metals were used in the form of chips. The desired mix of metals was melted in a vacuum arc melter, which was pumped down and backfilled with argon gas to minimize oxide/nitride formation. The chamber was then held at a positive pressure to mitigate the penetration of air into the chamber during the arc melting

process. Prior to melting each desired RMPEA composition in the argon - backfilled chamber, a lump of titanium metal was melted and allowed to cool down in the chamber to consume any residual nitrogen/oxygen present in the chamber, as titanium has a high affinity towards nitrogen and oxygen to form nitrides/oxides. Each RMPEA was melted and solidified three times, with the melted and solidified puck being flipped between each melting/solidification run to ensure homogeneous melting and mixing of all the constituent metals. The melted and solidified pucks, measuring 10 mm thick and 50–60 mm diameter, were sectioned and then analyzed under an optical microscope and subsequently scanning electron microscopy (SEM) – energy dispersive X-ray spectroscopy (EDS) to check for any un-melted chunks of constituent metal. If such a chunk was found, the whole puck was remelted. A metallographic sample was prepared from each composition for characterization of the as-cast microstructure.

2.2. Surface laser remelting and solidification

The as-cast pucks were then sectioned into thin (~3mm) slices. An in-house built additive manufacturing system was used to direct a laser beam (powered at 400 W) at the thin slices to re-melt the surfaces of the samples. In each laser remelting experiment, the sample was placed on a copper block, held in a vise, and mounted on a belt-driven system that facilitated motion in two directions in the horizontal plane. The system is contained in an airtight enclosure, which was flushed with Argon gas before remelting. During remelting, the sample moved at 200 mm/min to provide enough time to remelt the surface. There was a 50% overlap of the area scanned by the laser between adjacent passes. Passes were made on the sample until the whole surface was remelted and subsequently rapidly solidified. A stream of Argon gas flowed around the laser to prevent oxidation. A schematic of the laser remelting process is shown in Fig. 1. After the entire process, samples for metallographic observations were prepared.

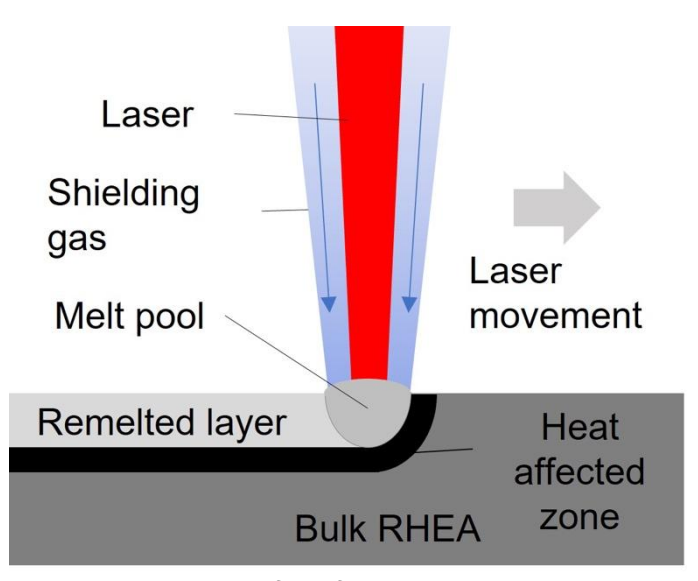


Figure 1. Schematic showing the process of surface laser remelting and solidification of bulk RMPEAs.

2.3. Oxidation

As-cast and laser remelted samples from each of the compositions were oxidized in a thermogravimetric analyzer. The samples were placed in a platinum crucible and suspended from a balance with a platinum wire. The temperature was ramped at 8 °C/min to the isothermal holding temperature of 1000 °C where the oxidation was carried out for 2 hours in a gas mixture of 17% O₂ and 83% helium (He) flowing at 500 ml/min. The thermal ramp and cooling down were carried out in He flowing at 1000 ml/min to avoid oxidation during these stages, so that pure isothermal oxidation can be studied. For microstructural characterization, the oxidized samples were mounted in a cold-cure epoxy puck and sectioned to reveal the interface between the base alloy and the oxide layer.

2.4. Characterization

Microstructural features and elemental distribution for as-cast and laser remelted samples were investigated using a Thermo Fisher Axia ChemiSEM. Hardness measurements on all samples were performed on a Struers Duramin 5 Microhardness tester at a load of 0.1 kg and a dwell time of 10 s. A low load of 0.1 kg was used in an effort to restrict the indentation to the surface layer, so as to isolate

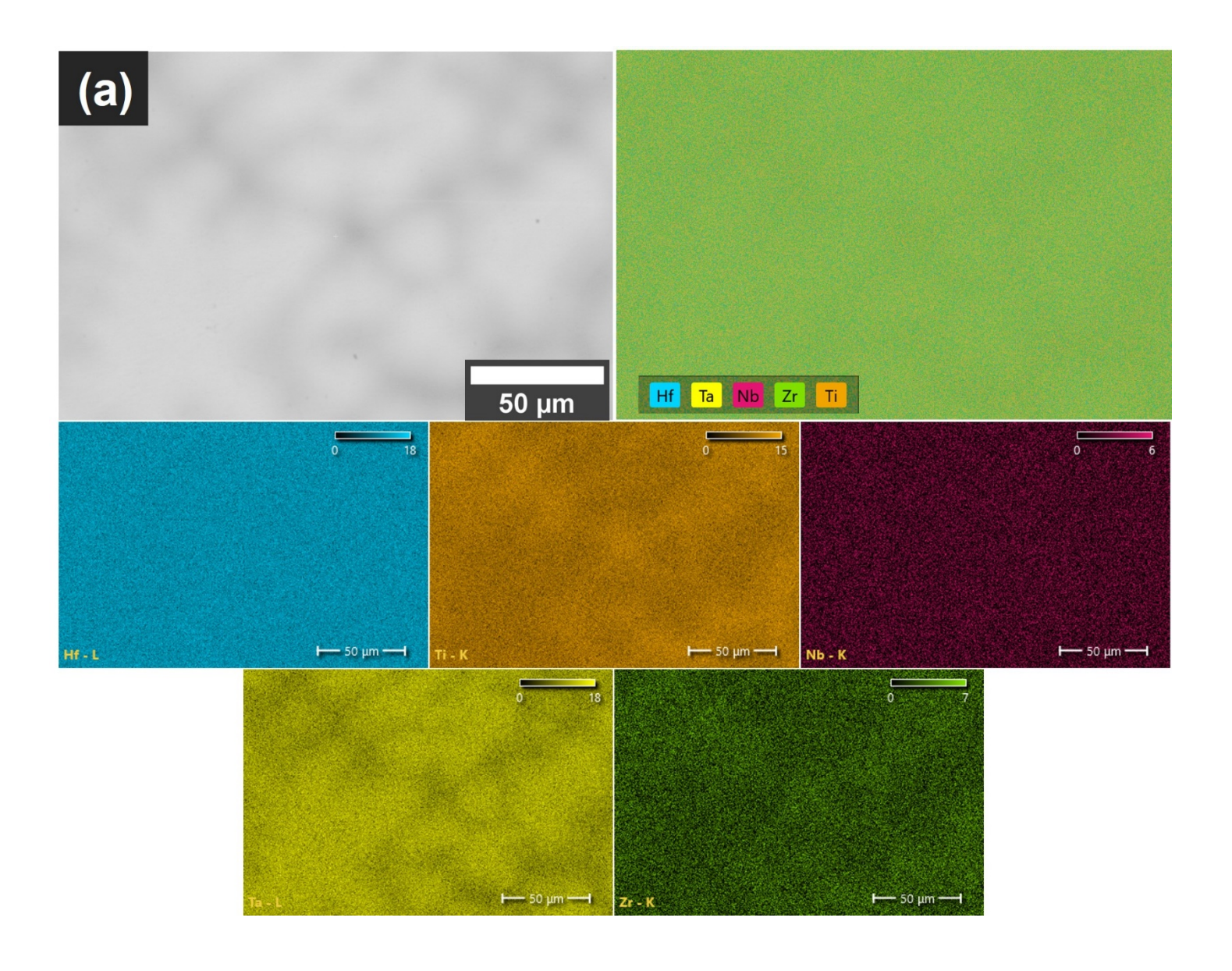
the effect of surface laser remelting. SEM micrographs and EDS elemental distribution maps of the oxidized samples were obtained using a Thermo Fisher Helios Hydra CX. X-ray diffraction (XRD) patterns were collected on the oxidized samples using a Philips MRD XRD with diffraction angles from 5 to 90° and a total scanning time of 30 min.

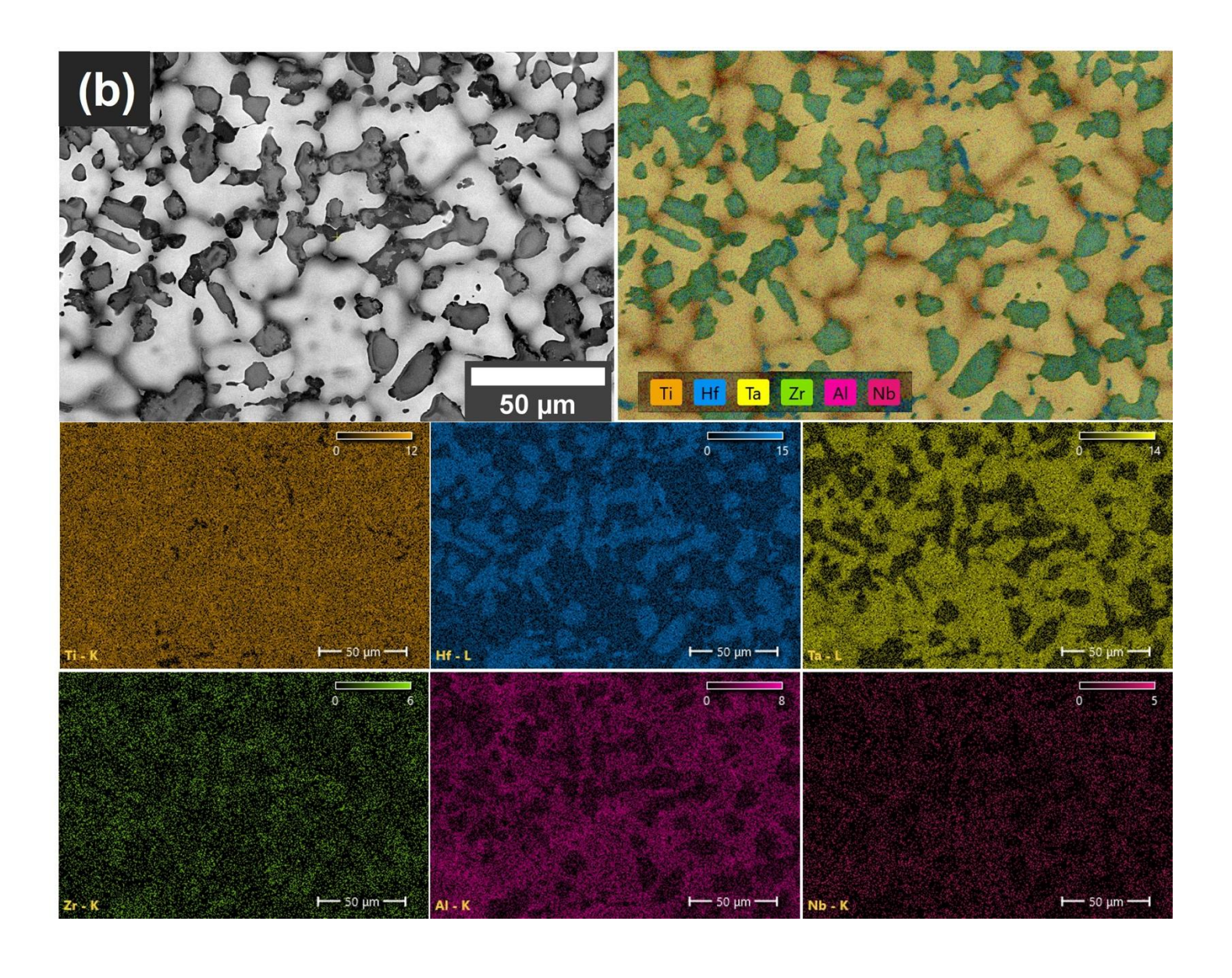
3. Results and discussion

3.1. Microstructural characterization

Figure 2. shows backscattered electron (BSE) SEM micrographs along with elemental distribution maps, obtained using EDS, for the as-cast samples of the three RMPEAs. Compositional data corresponding to these micrographs are presented in Table 1. For the base composition (C1), the BSE image (Fig. 1(a)) shows the presence of darker regions surrounding the grains, which may correspond to grain boundaries. The corresponding EDS maps show that the constituent elements are homogeneously distributed with a slight depletion of Nb and Ta at the grain boundaries. There is no evident enrichment of elements. Two-phase dendritic microstructures are observed in compositions containing Al and Cr in Fig. 1(b) and 1(c). The dendritic region in each of the compositions is enriched in Hf and Zr, whereas the inter-dendritic region is enriched in Nb and Ta. This segregation can be attributed to the difference in melting points of the elements and has been previously reported in similar RMPEA systems [13]. For the compositions C Al and C Cr, both Al and Cr are present in the brighter inter-dendritic phase with Ta and Nb. The preferential presence of Cr and Al in the inter-dendritic region with Ta and Nb can be explained in terms of the crystal structure of the corresponding elements. While group IV elements—i.e. Ti, Zr, and Hf—have a hexagonal closed packed structure, elements in group V (i.e., Ta and Nb), as well as Cr and Al, all possess a cubic crystal structure[14]. Apart from similarity in crystal structures, the atomic size of Al (143 pm) and Cr (129 pm) are closer to Nb (146 pm), and Ta (146 pm), than Ti (147 pm), Zr (160 pm), and Hf (159 pm)[14]. The electronegativity of Al (1.61) and Cr (1.66) is closer to Nb (1.60) and Ta (1.5) when compared with Zr (1.33) and Hf (1.30)[15]. Considering the Hume-Rothery Rules for the formation of substitutional solid solutions[16], identical crystal structure, as well as similar atomic radii and electronegativities of Al and Cr with Ta and Nb, explains why Al and Cr exist in the inter-dendritic region with Ta and Nb. Apart from the co-existence of Cr with Ta and Nb in the inter-dendritic region, a separate Cr-enriched dendritic phase is present in the C_Cr composition with Cr content measuring as high as 45 at.%. No such segregation was visible for the C Al composition.

Figure 3. displays BSE SEM micrographs of the laser remelted (LR) counterparts for the three RMPEA compositions. Even though the microstructural features in the laser remelted samples are like those in the as-cast samples, the scale of these features is significantly reduced. The micrograph for the LR-C1 in Fig. 3(a) shows the development of prominent dendrites as compared to the as-cast micrograph. From EDS results not shown here, these dendrites are also enriched in Zr and Hf with the inter-dendritic region being enriched in Nb and Ta. Ti is present in both these regions in approximately equal amounts. For the LR-C_AI (Fig. 3(b)), there is no significant difference as compared to the as-cast counterpart, other than reduction of scale of the microstructural features. The LR-C_Cr micrograph (Fig. 3(c)) points to the development of a nearly equiaxed structure intertwined with the pre-existing dendritic structure. Solute segregation is evident on the grain boundaries. For LR-C1, the dendrites seem to align in a particular direction, which is not seen in LR-C_Cr or LR-C_AI. Further investigations are required to understand the reason why the dendrites align in this particular fashion.





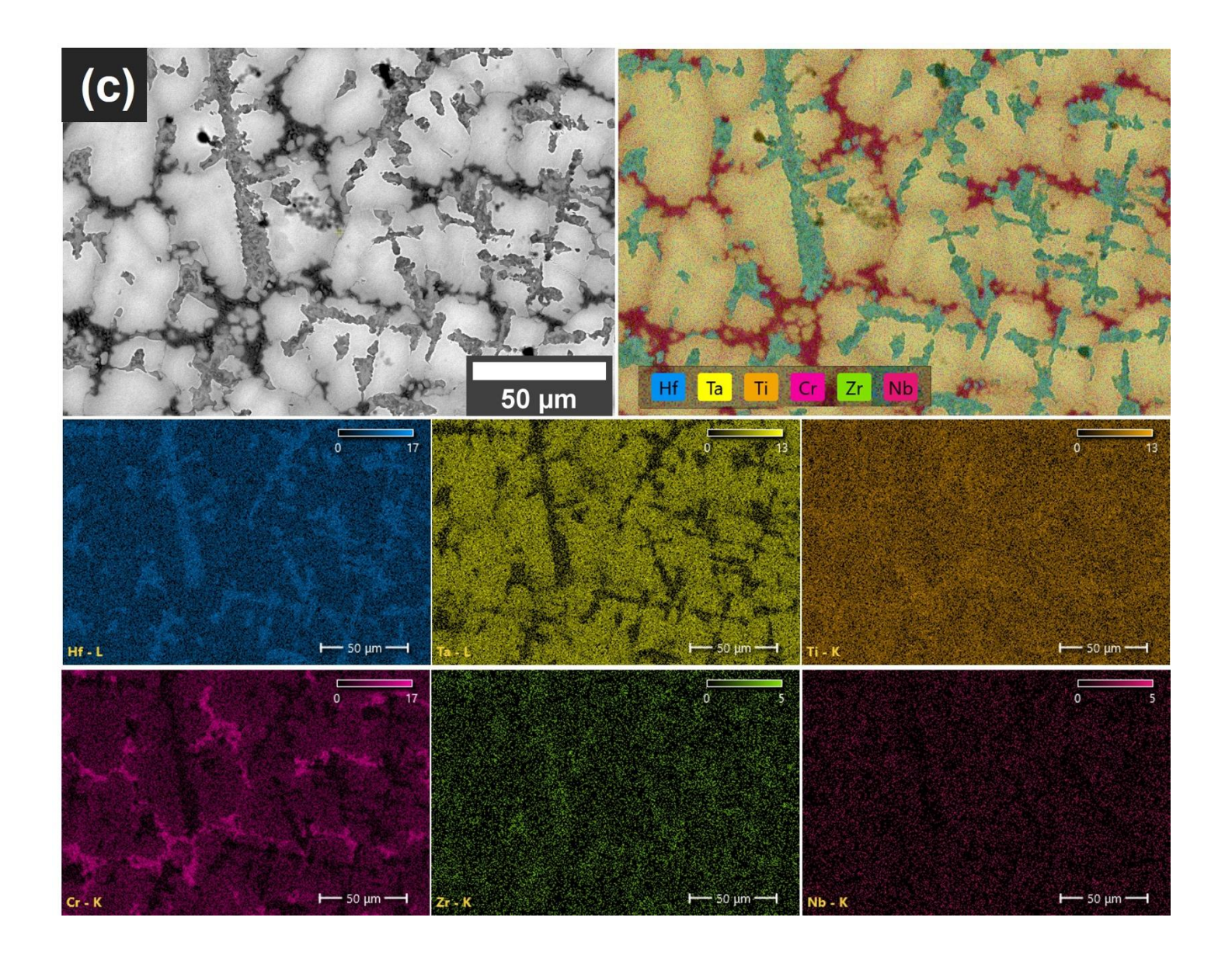


Figure 2. BSE SEM images showing the as-cast microstructures of the RMPEAs: (a) HfNbTaTiZr (C1); (b) (HfNbTaTiZr)₉AI (C_AI); (c) (HfNbTaTiZr)₉Cr (C_Cr). The elemental distribution maps obtained using EDS for all the compositions are also included. The presence of two distinct phases is clearly visible in AI- and Cr- containing compositions.

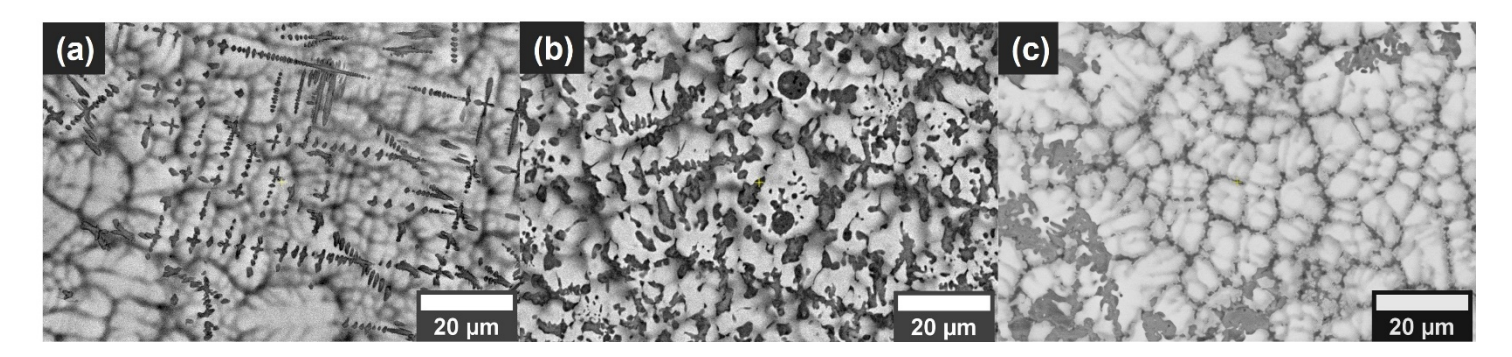


Figure 3. BSE SEM images showing laser remelted microstructures of the (a) C1 (b) C_AI, and (c) C_Cr compositions. The presence of finer microstructural features is visually evident with dendritic and interdendritic regions in (a) and (b). (c) exhibits an equiaxed structure intertwined with the former dendritic structure.

Table 1. The as-cast compositions of the three RMPEA systems as determined using energy dispersive spectroscopy (EDS). The compositions presented are overall compositions determined using multiple area scans, which confirm that the desired compositions were attained.

Composition	Atomic %						
	Hf	Nb	Та	Ti	Zr	Al	Cr
HfNbTaTiZr	20.5	20.8	18.8	19.1	19.8	-	-
(HfNbTaTiZr) ₉ Al	17.0	18.2	17.7	18.3	17.9	10.8	-
(HfNbTaTiZr) ₉ Cr	18.7	17.1	17.2	18.1	18.7	-	10.2

3.2. Hardness

The hardness of the as-cast and laser remelted RMPEAs is presented in Fig. 4. From the figure, the base quinary composition (C1) has the lowest hardness for both as-cast and laser remelted counterparts. The hardness of all the senary compositions is higher than that of the base quinary composition. This can be attributed to the increased compositional complexity due to the addition of the sixth element. Previously, it has been shown that compositional complexity leads to increased dislocation density [17,18].

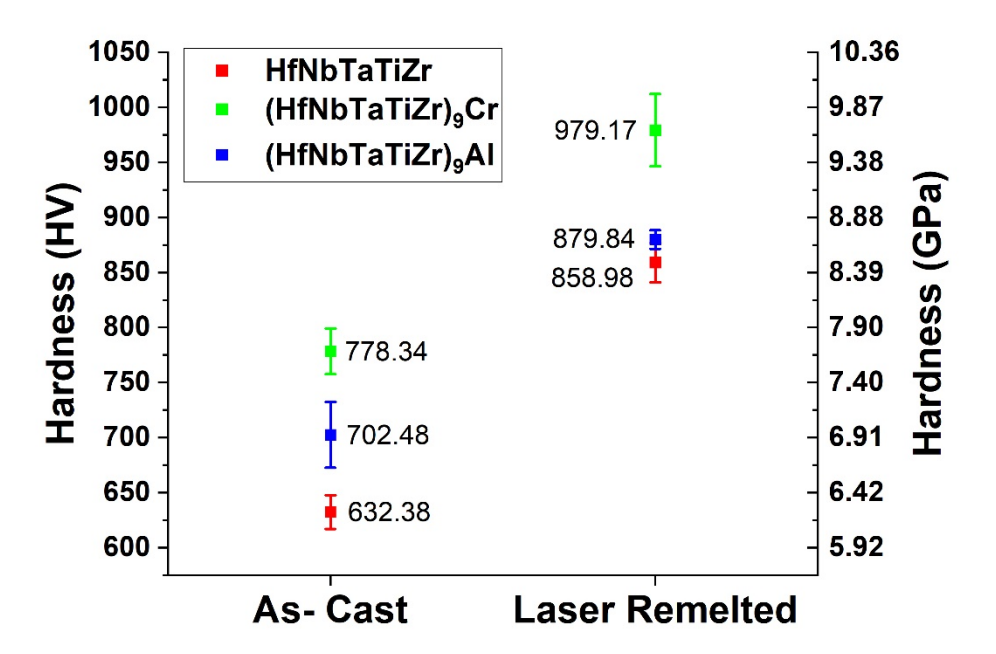


Figure 4. Graph depicting the variation of hardness with respect to composition as well as the processing route. Laser remelting the RMPEAs led to an increase of ~30% in hardness for all three systems.

Apart from that, in MPEAs, the atomic heterogeneity, i.e. the random distribution of constituent elements with varying sizes on lattice sites, induces lattice distortion. This acts as an obstacle towards dislocation

motion during plastic deformation. Previous studies have emphasized the role that atomic size misfit plays towards lattice distortion [19–22]. Therefore, the lattice distortion is proportional to the atomic size misfit (δ), which can be calculated as shown in Eq. 1:

$$\delta = 100\sqrt{\sum_{i=1}^{n} c_i \left(1 - \frac{r_i}{\bar{r}}\right)^2} \tag{1}$$

where c_i is the concentration of individual atomic species, r_i is the radius of that species, and \bar{r} is the average atomic radius. Using the values of atomic radii as previously mentioned in section 3.1, the atomic size misfit for compositions C1, C_Al and C_Cr is 4.27%, 4.45% and 6.27%, respectively, as calculated using Eq. 1. Since the atomic size misfit for senary compositions is greater than for quinary composition, the lattice distortion will be greater in senary compositions. Two determining factors for hardness of polycrystalline materials are dislocation density and barriers for dislocation motion. Hence, a combination of increased dislocation density and higher resistance to dislocation motion—as a result of higher lattice distortion—in senary compositions results in higher hardness compared to quinary composition, C1. In a previous study [23] that investigated the effect of compositional complexity on lattice distortion in the FeNiCoCrMn MPEA system (Ni, FeNi, FeNiCo, FeNiCoCr, FeNiCoCrMn), it was shown that the significant lattice distortion is absent due to the smaller magnitude of atomic size misfit of < 1.12%. Therefore, the hardness of the system showed narrow variation as the compositional complexity was increased. Even though atomic size misfit is not the only factor that contributes towards lattice distortion, it is supported by previous studies that atomic size misfit can be confidently correlated to the lattice distortion for such systems [21].

Based on the cocktail effect in MPEAs, where the interactions between the constituent elements have a composite effect on the properties of the alloys, the difference between the hardness values of

senary compositions may be explained by the difference in the individual hardness of the sixth element added to the quinary composition. The individual Vickers hardness value of Cr and Al are 1060 HV and 167 HV, respectively [14], and thus, the variation in the hardness values of the corresponding senary RMPEAs.

Even though the hardness among the laser remelted compositions follows the same trend as the as-cast samples, there are increases in hardness as compared to the as-cast compositions by ~30%. This increase in hardness can be attributed to the reduction in scale of the microstructural features in Fig. 3 when compared to Fig. 2, as a result of laser-remelting [24–27]. This increase in hardness may be explained by the Hall-Petch-type relation [28,29]. In the Hall-Petch relation, the yield strength of a material is directly related to the grain size. Since hardness is the measure of a material's ability to resist localized deformation or "yielding," the hardness of the material is inversely related to the grain size. It is a well-established fact via prior studies [30–33] that there is an increase in hardness as the grain size of the material decreases. In other studies [24,25,27,34,35], an improvement in the hardness and other mechanical properties has also been indicated as a result of laser remelting. In this study, quantification of grain sizes in the as-cast and laser-remelted samples is difficult due to the dendritic microstructures in both types of samples, and therefore quantitative calculations using the Hall-Petch relation were not performed. However, the grain sizes of the as-cast samples and laser-remelted samples were estimated to be ~80-120 μm and ~5-10 μm, respectively.

3.3 Oxidation

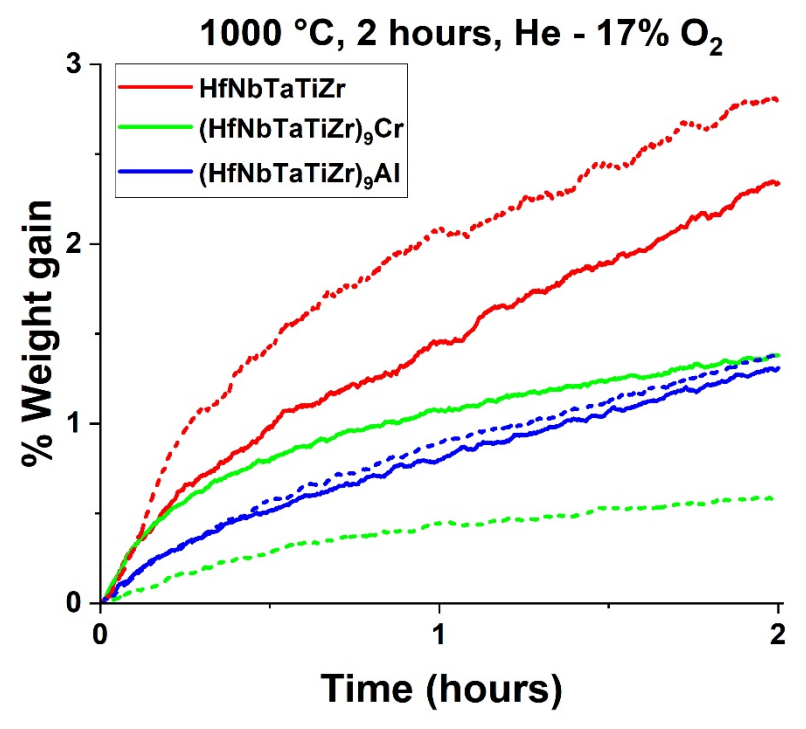
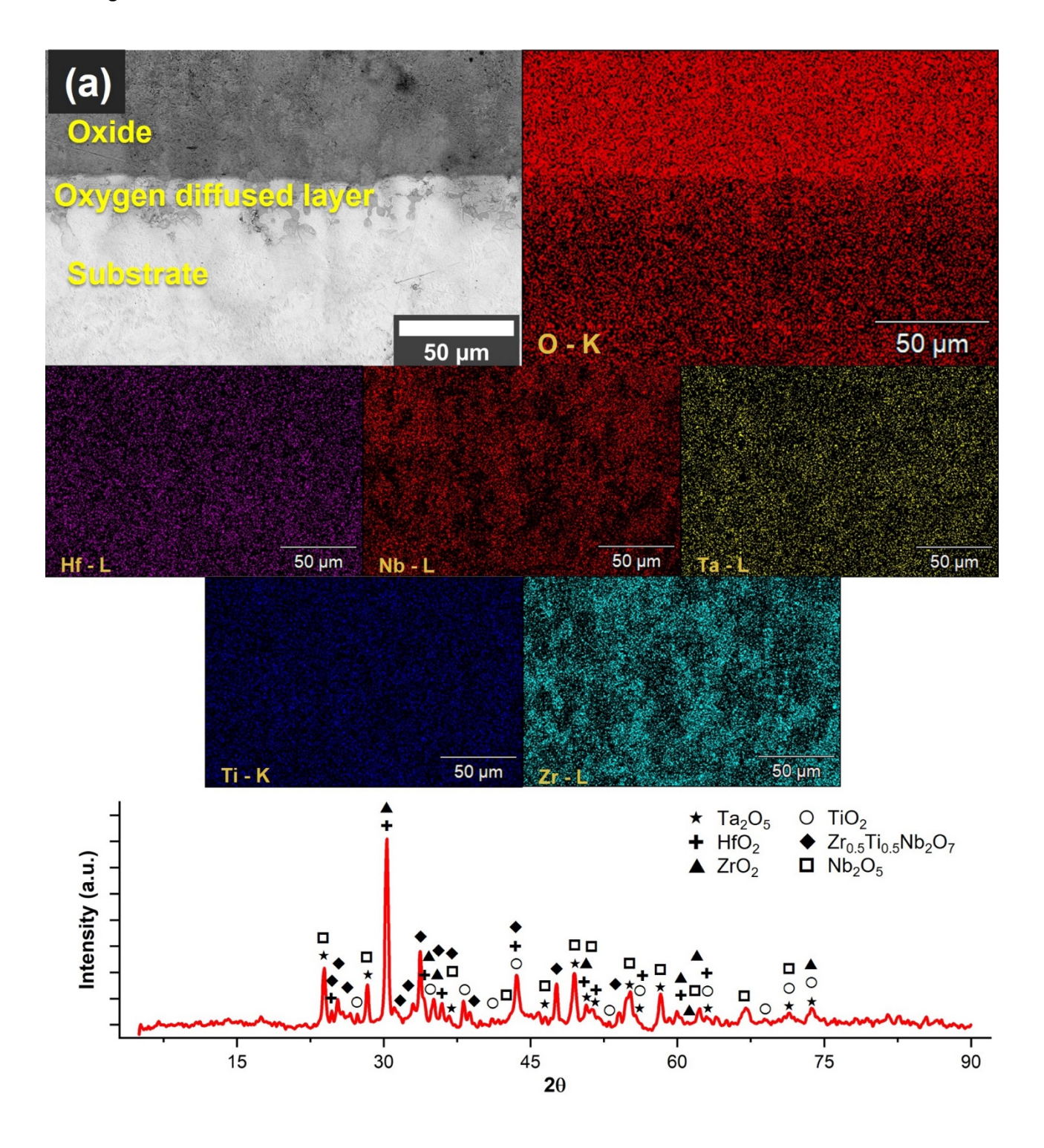
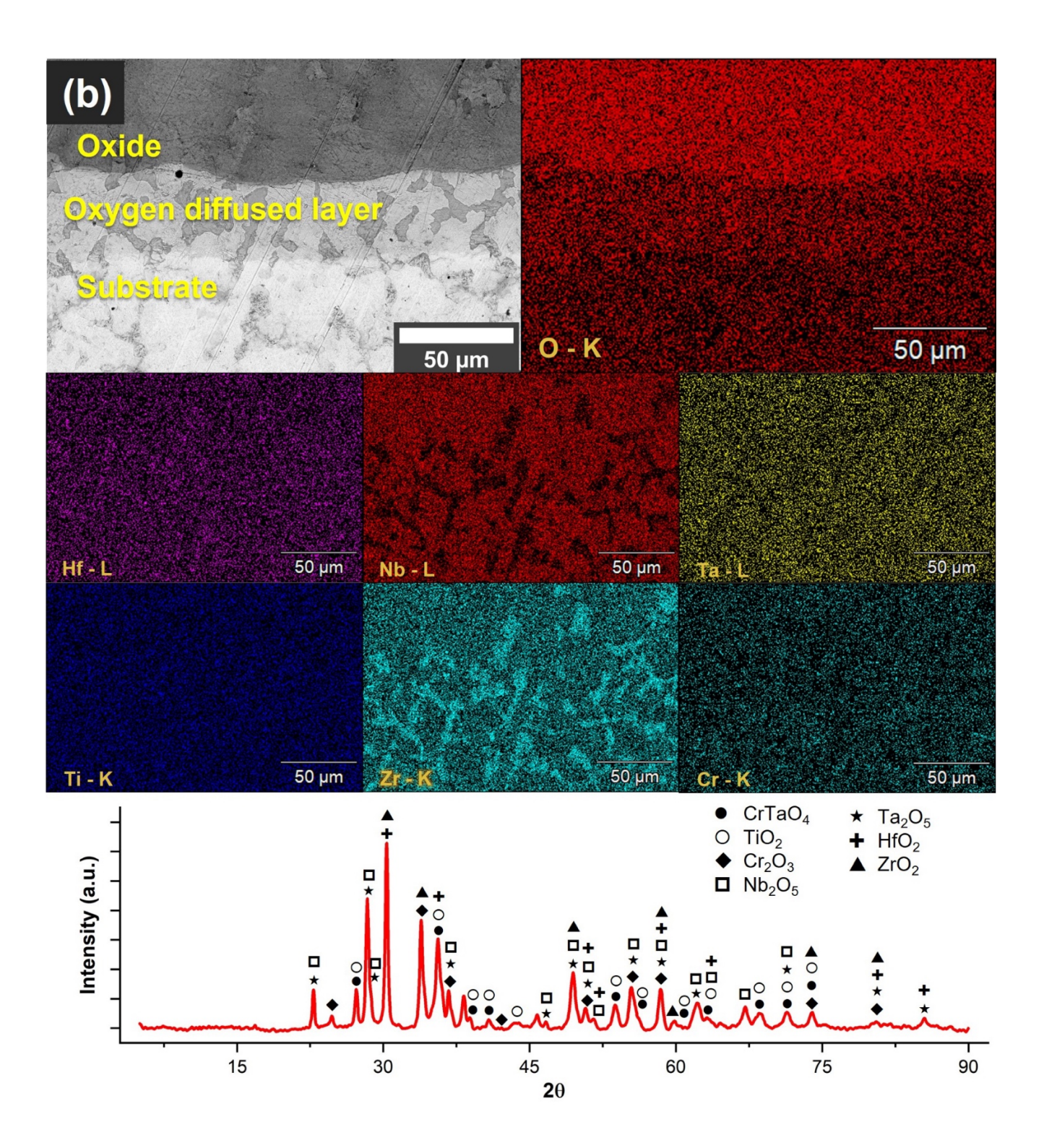


Figure 5. Weight% gain with respect to time for the different compositions of RMPEAs. Comparisons between the as-cast and laser remelted samples are also shown. Solid lines represent as-cast samples, and the dashed lines correspond to the laser-remelted samples.

Figure 5 shows the weight% gained vs. time of oxidation for both the as-cast and laser remelted counterparts for each of the three RMPEA compositions. Each weight gain profile is an average of two oxidation runs for improved accuracy. After two hours of oxidation at 1000 °C, the as-cast samples exhibit a weight gain of 2.34% for C1, 1.31% for C_AI, and 1.38% for C_Cr. This implies that the addition of the sixth element to the quinary composition C1 has an overall positive effect in terms of oxidation resistance. From the weight gain profile for the three systems, it can be inferred that while the weight gain profiles for C1 and C_AI show an upward trending profile after 2 hours, the C_Cr system's profile seems to have plateaued out already after 2 hours. Thus, it may be hypothesized that even though the

C_Al system has a marginally better oxidation resistance at 2 hours as compared to the C_Cr system, the C_Cr system may have better oxidation resistance than the C_Al system at longer exposure to oxidizing conditions.





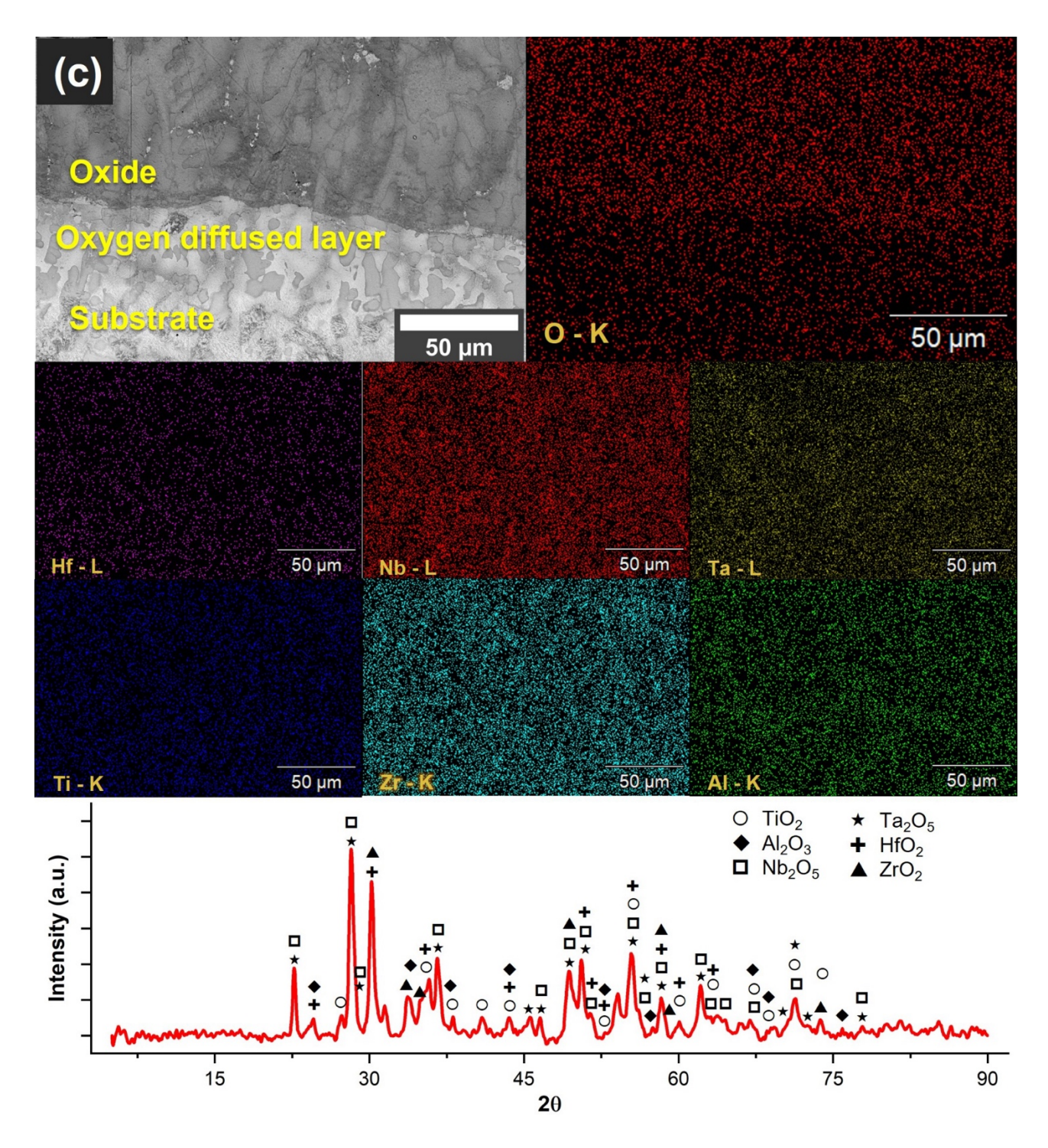


Figure 6. BSE SEM images showing the cross section of the as-cast microstructures of the RMPEAs after oxidation at 1000 °C in 17% O_2 for 2 hours: (a) HfNbTaTiZr (C1); (b) (HfNbTaTiZr) $_9$ Cr (C_Cr); (c) (HfNbTaTiZr) $_9$ Al (C_Al). The elemental distribution maps obtained using EDS for all the compositions are included. The oxide layer, oxygen diffusion zone, and substrate are indicated in the cross-section.

The variation in contrast in the oxide layers indicates that there are multiple oxide phases present. In each sample, the XRD pattern obtained from the oxide layer indicates the presence of mixed (complex) oxides.

Figure 6 displays the BSE images and EDS elemental maps of the cross section for the three ascast alloys after oxidation at 1000 °C in 17% O₂ for 2 hours. The BSE images show a thick oxide layer, a thin oxygen-diffused layer followed by the substrate for all three compositions. The contrast in the oxide layer reveals the presence of compositional inhomogeneity in the layer, for each of the three compositions. Like the as-cast C Al and C Cr alloys, the EDS maps indicate that there is segregation between Zr, Hf and Nb, Ta in the three systems. For each composition, the XRD pattern obtained from the oxide layer indicates the presence of complex mixed oxides. The guinary composition shows the formation of complex, mixed oxides (Fig. 6(a)). The presence of Hf, Zr and Nb is known to have detrimental effects on the protective nature of an oxide layer. RMPEA containing Hf tends to undergo pesting because of increased volume of the oxide layer [36]. Zr upon oxidation leads to the formation of a fast growing ZrO₂ [37]. Oxidation of Nb can lead to the formation of oxides with increased porosity and, accordingly, spallation of the oxide layer [38]. For the C Cr senary composition, the oxide layer contains mixed oxides as well as the CrTaO₄ complex oxide as indexed in the XRD pattern in Fig. 6(b). Cr exhibits a preferential presence with Ta in the substrate as well as the oxide layer as can be seen from the elemental maps. Previous studies have shown that the addition of Cr to steels as well as MPEA systems leads to an enhancement of oxidation resistance [39-42]. In steels [43-45], Cr enhances oxidation resistance because of the formation of a dense, protective Cr₂O₃ layer. However, the existence of such a layer was not seen in MPEA systems where the addition of Cr led to a similar positive effect [46,47]. In some cases, the protective chromium oxide layer can be a few nanometers

thick [48] and therefore, in this study, the existence of such a layer was not observed due to the limited resolving power of the SEM used. Even though the existence of a Cr-enriched or Cr₂O₃ layer is not evident, the absence of Cr-enriched dendrites in the substrate for the oxidized C_Cr sample (which is in contrast with the presence of such Cr-enriched dendrites in the as-cast counterpart) may indicate that there is preferential Cr oxidation. It can be hypothesized that even though a dense chromium oxide layer is not visible, the passivating effect is due to the presence of Cr oxide in the mixed oxide layer.

Similarly, for C_AI the oxide layer consists of a mixture of oxides as shown in the XRD pattern in Fig. 6(c); the presence of an oxygen diffusion zone is also indicated in the SEM image in Fig. 6(c). As in the case of C_Cr, previous studies have established that enhancement in oxidation resistance can also be aided by the addition of AI to MPEAs [42,49,50]. Chang *et al.*, [51] investigated the effects of AI addition to C1 in percentages different than what is being investigated in this study. It was observed that with an increase in the AI content, the oxidation resistance of the RMPEA system improved. However, in contrast to Cr₂O₃, the formation of AI₂O₃ does not have any additional benefits such as suppressing the formation of other detrimental oxides (such as Nb₂O₅). Furthermore, in a Nb-containing RMPEA, AI₂O₃ is known to form low melting eutectics upon reaction with oxides such as Nb₂O₅ [52], which can hinder the alloy's ability to be used at high temperatures where corrosion also occurs. Fig. S1 in the supplementary materials shows the micrographs with the complete oxide scale (refer to online supplementary material).

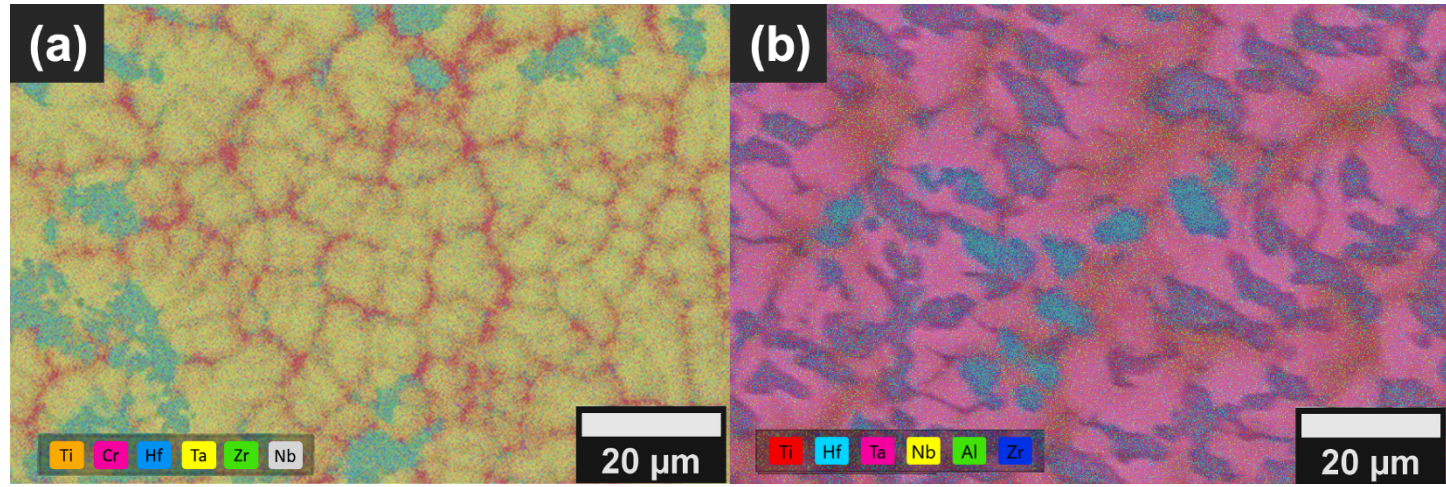


Figure 7. EDS maps of the laser remelted (a) C_Cr and (b) C_Al. Segregation of chromium is apparent at the grain boundaries in (a). No such segregation is visible in (b). Cr elemental distribution map is shown in Figure S2.

After laser remelting (LR), the RMPEAs show an interesting variation in oxidation resistance. Firstly, after laser remelting, the microstructural features diminish in size, thus increasing the total grain boundary area. This allows for enhanced diffusion of the oxidant and the alloying elements, as diffusion through grain boundary is faster than diffusion through the bulk [53]. Faster diffusion of the oxidant/alloying elements leads to faster oxidation. Owing to this faster diffusion of oxidants through the increased grain boundary area in the laser remelted C1 quinary composition, a decline in the oxidation resistance is observed. After oxidation, the LR-C1 composition gained 19.65% more weight, calculated as (difference in weight gain of the LR and as-cast sample × 100%) / weight gained by the as-cast sample, as compared to the weight gained by the as-cast sample. Secondly, the presence of elements, which form a passivating oxide, along these grain boundaries accelerate the formation of protective oxides upon diffusion via the increased grain boundaries, thus overall slowing down oxidation. Laser remelting C_Cr leads to enhancement in oxidation resistance. In Fig. 7, it is evident that there is Cr segregation at the grain boundaries along the equiaxed grains in the laser remelted

C_Cr sample. A Cr-only elemental distribution map in Fig. S2 shows the segregation along the grain boundaries. In this case, the faster grain boundary diffusion coupled with the presence of Cr, which tends to form passivating oxide, along the grain boundaries, improves the oxidation resistance in comparison to the as-cast sample of the same composition [54,55]. Wang *et al.*, indicated that grain refinement in Ni-based alloys led to enhanced diffusion of Cr [56]. After oxidation, the LR-C_Cr senary composition gained 42% less weight as compared to the as-cast counterpart. Thirdly, in the case of LR-C_AI, there is no segregation of AI along the grain boundaries (as seen in Fig. 7 (b)). Thus, even though the AI forms a passivating oxide layer [49,51,54], the enhanced oxidation as a result of faster grain boundary diffusion of other non-passivating elements negates the benefit brought by AI; eventually laser remelting barely changed the oxidation resistance of C_AI, and the oxidation resistance of LR-C_AI is not as good as that of LR-C_Cr.

4. Conclusions

In this study, we investigated the effect of laser remelting for the HfNbTaTiZr refractory multi-principal element alloy systems on the microstructure, hardness, and oxidation resistance. Effects of Al and Cr additions were also investigated on the aforementioned parameters coupled with laser remelting. Based on the obtained results and analysis, the following conclusions can be drawn:

- 1. Laser remelting led to the development of finer microstructure in all the three compositions, HfNbTaTiZr, (HfNbTaTiZr)₉Cr and (HfNbTaTiZr)₉Al, as is expected during additive manufacturing.
- 2. Compositional complexity and degree of atomic size misfit played a role in the increment of hardness of the senary compositions in comparison with the quinary composition. The difference between the hardness of the two senary compositions is due to the difference in hardness of the constituent elements, thereby the hardness trend being (HfNbTaTiZr)₉Cr > (HfNbTaTiZr)₉Al >

- HfNbTaTiZr. A hardness increment of 30% for all the compositions was achieved after laser remelting when compared with as-cast samples. This can be explained by the Hall Petch relation.
- 3. The presence of elements forming passivating oxides can lead to higher oxidation resistance. For both the as-cast and laser remelted conditions, the oxidation resistance of (HfNbTaTiZr)₉Cr or (HfNbTaTiZr)₉Al is better than that of HfNbTaTiZr.
- 4. Oxidation resistance may be enhanced, barely changed, or diminished after laser remelting depending on the composition. For (HfNbTaTiZr)₉Cr, the oxidation resistance was improved, and weight gain after oxidation for the laser remelted sample was reduced by 42% when compared with that for the as-cast counterpart. This phenomenon can be attributed to the segregation of Cr at the grain boundaries with increased area, and to the fast diffusion of Cr along the grain boundaries and accordingly preferential oxidation of Cr to form protective oxides. In the case of (HfNbTaTiZr)₉AI, laser remelting did not have any noticeable effect on the oxidation resistance. For HfNbTaTiZr, laser melting caused the oxidation resistance to diminish.

5. ACKNOWLEDGMENTS

This research was supported by a seed grant from the Intelligent Systems Center of Missouri University of Science and Technology and by a research grant (award number 2207965) from the U.S. National Science Foundation. The Materials Research Center at Missouri University of Science and Technology is acknowledged for providing access to electron microscopy and X-ray diffraction. Dr. Eric Bohannan is thanked for his assistance with X-ray diffraction.

6. CONFLICT OF INTEREST

On behalf of all authors, the corresponding author states that there is no conflict of interest.

7. REFERENCES

- 1. O. N. Senkov, G. B. Wilks, D. B. Miracle, C. P. Chuang, and P. K. Liaw, Intermetallics 18, 1758 (2010).
- 2. J. P. Couzinié, G. Dirras, L. Perrière, T. Chauveau, E. Leroy, Y. Champion, and I. Guillot, Mater. Lett. 126, 285 (2014).
- 3. M. C. Gao, B. Zhang, S. Yang, and S. M. Guo, Metall. Mater. Trans. A Phys. Metall. Mater. Sci. 47, 3333 (2016).
- 4. B. Liu, J. Wang, J. Chen, Q. Fang, and Y. Liu, JOM 69, 651 (2017).
- 5. O. A. Waseem, J. Lee, H. M. Lee, and H. J. Ryu, Mater. Chem. Phys. 210, 87 (2018).
- 6. B. Kang, J. Lee, H. J. Ryu, and S. H. Hong, Mater. Sci. Eng. A 712, 616 (2018).
- 7. H. Dobbelstein, E. P. George, E. L. Gurevich, A. Kostka, A. Ostendorf, and G. Laplanche, Int. J. Extrem. Manuf. 3, 15201 (2020).
- 8. R. Wang, K. Zhang, C. Davies, and X. Wu, J. Alloys. Compd. 694, 971 (2017).
- 9. H. I. Jeong, C. M. Lee, and D. H. Kim, Mater. 15, 6570 (2022).
- 10. H. Dobbelstein, E. L. Gurevich, E. P. George, A. Ostendorf, and G. Laplanche, Addit. Manuf. 24, 386 (2018).
- 11. H. Dobbelstein, M. Thiele, E. L. Gurevich, E. P. George, and A. Ostendorf, Phys. Procedia. 83, 624 (2016).
- 12. B. Xiao, W. Jia, J. Wang, and L. Zhou, Mater. Charact. 193, 112278 (2022).
- 13. C. C. Juan, M. H. Tsai, C. W. Tsai, C. M. Lin, W. R. Wang, C. C. Yang, S. K. Chen, S. J. Lin, and J. W. Yeh, Intermetallics 62, 76 (2015).

- 14. G.V. Samsonov, *Handbook of the Physicochemical Properties of the Elements*, (Springer New York, NY, 2012) pp. 97 124.
- 15. "Periodic Table Ptable Properties Electronegativity." https://ptable.com/?lang=en#Properties/Electronegativity (accessed Apr. 20, 2023)
- 16. W. Hume-Rothery, J. Inst. Met. 35, 295 (1926).
- 17. P. Thirathipviwat, G. Song, J. Jayaraj, J. Bednarcik, H. Wendrock, T. Gemming, J. Freudenberger, K. Nielsch, and J. Han, J. Alloys. Compd. 790, 266 (2019).
- 18. P. Thirathipviwat, G. Song, J. Bednarcik, U. Kühn, T. Gemming, K. Nielsch, and J. Han, Prog. Nat. Sci. Mater. Int. 30, 545 (2020).
- 19. Q. Ding, Y. Zhang, X. Chen, X. Fu, D. Chen, S. Chen, L. Gu, F. Wei, H. Bei, Y. Gao, M. Wen, J. Li, Z. Zhang, T. Zhu, R. O. Ritchie, and Q. Yu, Nat. 574:7777 574, 223 (2019).
- 20. C. Lee, G. Song, M. C. Gao, R. Feng, P. Chen, J. Brechtl, Y. Chen, K. An, W. Guo, J. D. Poplawsky, S. Li, A. T. Samaei, W. Chen, A. Hu, H. Choo, and P. K. Liaw, Acta. Mater. 160, 158 (2018).
- 21. H. Song, F. Tian, Q. M. Hu, L. Vitos, Y. Wang, J. Shen, and N. Chen, Phys. Rev. Mater. 1, 023404 (2017).
- 22. P. Thirathipviwat, S. Sato, G. Song, J. Bednarcik, K. Nielsch, J. Jung, and J. Han, Scr. Mater. 210, 114470 (2022).
- 23. P. Thirathipviwat, S. Sato, G. Song, J. Bednarcik, K. Nielsch, and J. Han, Mater. Sci. Eng. A 823, 141775 (2021).
- 24. T. Han, Y. Liu, M. Liao, D. Yang, N. Qu, Z. Lai, and J. Zhu, J. Mater. Sci. Technol. 99, 18 (2022).
- 25. S. Zhou, Y. Xu, B. Liao, Y. Sun, X. Dai, J. Yang, and Z. Li, Opt. Laser. Technol. 103, 8 (2018).
- 26. K. Yang, J. Li, Q. Y. Wang, Z. Li, Y. Jiang, and Y. Bao, Wear 426-427, 314 (2019).
- 27. X. Yang, J. Liu, X. Cui, G. Jin, Z. Liu, Y. Chen, and X. Feng, J. Phys. Chem. Solids. 130, 210 (2019).

- 28. I. Watanabe, K. Terada, and M. Akiyama, J. Iron Steel Inst. 174, 25 (1953).
- 29. E. Hall, Proc. Phys. Soc. Sect. B 64, 747 (1951).
- 30. X. B. Feng, J. Y. Zhang, Y. Q. Wang, Z. Q. Hou, K. Wu, G. Liu, and J. Sun, Int. J. Plast. 95, 264 (2017).
- 31. H. X. Yang, J. S. Li, T. Guo, W. Y. Wang, H. C. Kou, and J. Wang, Rare Met. 39, 156 (2020).
- 32. J. Gubicza, A. Heczel, M. Kawasaki, J. K. Han, Y. Zhao, Y. Xue, S. Huang, and J. L. Lábár, J. Alloys. Compd. 788, 318 (2019).
- 33. B. Gwalani, V. Soni, M. Lee, S. A. Mantri, Y. Ren, and R. Banerjee, Mater. Des. 121, 254 (2017).
- 34. C. Yao, P. Xiaotong, G. Qunfu, W. Zhijie, and N. Pulin, Mater. Sci. Eng. A 840, 142951 (2022).
- 35. B. Xin, X. Zhou, G. Cheng, J. Yao, and Y. Gong, Opt. Laser. Technol. 127, 106087 (2020).
- 36. S. Sheikh, M. K. Bijaksana, A. Motallebzadeh, S. Shafeie, A. Lozinko, L. Gan, T. K. Tsao, U. Klement, D. Canadinc, H. Murakami, and S. Guo, Intermetallics 97, 58 (2018).
- 37. N. Yurchenko, E. Panina, S. Zherebtsov, G. Salishchev, and N. Stepanov, Mater. 11, 2526 (2018).
- 38. F. Müller, B. Gorr, H. J. Christ, J. Müller, B. Butz, H. Chen, A. Kauffmann, and M. Heilmaier, Corros. Sci. 159, 108161 (2019).
- 39. S. Yang, W. Yu, T. Liu, C. Li, Y. Zhang, and Y. Qu, Mater. Res. Express. 6, 076501 (2019).
- 40. J. D. Roach, J. Electrochem. Soc. 98, 160 (1951).
- 41. B. Sun, X. Zuo, X. Cheng, and X. Li, npj Mater. Degrad. 4, 1 (2020).
- 42. B. G. Kim, G. M. Kim, and C. J. Kim, Scr. Metall. Mater. 33, 1117 (1995).
- 43. I. Saeki, H. Konno, R. Furuichi, T. Nakamura, K. Mabuchi, and M. Itoh, Corros. Sci. 40, 191 (1998).
- 44. Z. F. Li, G. M. Cao, Y. Q. He, Z. Y. Liu, and G. D. Wang, Steel. Res. Int. 87, 1469 (2016).
- 45. R. C. Lobb and H. E. Evans, Corros. Sci. 23, 55 (1983).
- 46. G. R. Holcomb, J. Tylczak, and C. Carney, JOM 67, 2326 (2015).

- 47. Y. Zhang, H. Wu, X. Yu, and D. Tang, Corros. Sci. 200, 110211 (2022).
- 48. T. Ohmi, Y. Nakagawa, M. Nakamura, A. Ohki, and T. Koyama, J. Vac. Sci. Technol. A 14, 2505 (1996).
- 49. Y. Y. Liu, Z. Chen, Y. Z. Chen, J. C. Shi, Z. Y. Wang, S. Wang, and F. Liu, Vacuum 169, 108837 (2019).
- 50. Z. G. Zhang, X. Teng, Y. L. Mao, C. X. Cao, S. J. Wang, and L. Wang, Oxid. Met. 73, 455 (2010).
- 51. C. H. Chang, M. S. Titus, and J. W. Yeh, Adv. Eng. Mater. 20, 1700948 (2018).
- 52. R. Serrazina, J. S. Dean, I. M. Reaney, L. Pereira, P. M. Vilarinho, and A. M. O. R. Senos, J. Mater. Chem. C. 7, 14334 (2019).
- 53. N. L. Peterson, Int. Met. Rev. 28, 65 (2013).
- 54. C. Kaplin and M. Brochu, Appl. Surf. Sci. 301, 258 (2014).
- 55. L. Liu, Z. gang Yang, C. Zhang, M. Ueda, K. Kawamura, and T. Maruyama, Corros. Sci. 91, 195 (2015).
- 56. X. Wang and J. A. Szpunar, J. Alloys. Compd. 752, 40 (2018).